# Eliminating the dipole phase in attosecond pulse characterization using Rydberg wave packets

Stefan Pabst and Jan Marcus Dahlström

Phys. Rev. A **94**, 013411 — Published 15 July 2016

DOI: 10.1103/PhysRevA.94.013411

# Eliminating the dipole phase in attosecond pulse characterization using Rydberg wave packets

Stefan Pabst[1,2,*] and Jan Marcus Dahlström[1,3,†]

[1] *ITAMP, Harvard-Smithsonian Center for Astrophysics, 60 Garden Street, Cambridge, MA 02138, USA*
[2] *Physics Department, Harvard University, 17 Oxford Street, Cambridge, Massachusetts 02138, USA*
[3] *Department of Physics, Stockholm University, AlbaNova University Center, SE-106 91 Stockholm*

We propose a new technique to fully characterize the temporal structure of extreme ultraviolet pulses by ionizing a bound coherent electronic wave packet. The influence of the dipole phase, which is the main obstacle for state-of-the-art pulse characterization schemes, can be eliminated by angle integration of the photoelectron spectrum. We show that particularly atomic Rydberg wave packets are ideal and that wave packets involving multiple electronic states provide redundant information which can be used to cross-check the consistency of the phase reconstruction.

## I. INTRODUCTION

Ultrafast optics allows for generation of laser pulses with durations on the femtosecond time scale. The pulses are shorter than the response time of any photodetector but limited by the femtosecond period of optical light. Methods to reconstruct laser pulses have been developed using nonlinear optical effects and cross correlation [1]. In 2001 the femtosecond barrier was broken by the generation of attosecond pulses in the (extreme) ultraviolet (UV) range in the form of isolated pulses [2] and pulse trains [3]. This signaled the start of a new era of ultrafast experiments, known as attosecond physics [4].

Today, the use of attosecond pulses allows for direct measurement of optical laser pulses on the femtosecond time scale [5], but the generation and characterization of attosecond pulses remains an active field of research [6]. Established techniques from ultra-fast nonlinear optics cannot be extended into the UV regime due to two main reasons: (i) low photon fluxes associated with the UV pulses do not favor nonlinear processes and (ii) high photon energies generally leads to target-dependent complex-valued susceptibilities that may obscure the field-reconstruction procedure. Therefore, all current attosecond characterization techniques instead rely on laser-dressed photoionization by near-infrared (NIR) fields [7]. Indeed, this is the principle of the FROG-CRAB-method [8], where the frequency-resolved optical gating (FROG)-algorithm from nonlinear optics [9, 10] is adapted as a phase gate given by the laser dressed continuum. If the IR field that dresses the continuum is weak then the signal can be analyzed in term of the phase retrieval by omega oscillation filtering (PROOF)-method [11].

In the above mentioned attosecond pulse characterization techniques, the dipole phases of bound–continuum and continuum–continuum transitions are neglected in the spirit of the strong field approximation [12]. However, relative ionization delay measurements have now shown that such atomic effects are important and can lead to delays up to a hundred attoseconds in solid state targets [13] and noble gas atoms [14–17]. The Wigner time delay of the photoelectron wave packet, defined as the energy-derivative of the bound–continuum dipole phase, depends on the atomic structure and typically varies by several as/eV [18]. The continuum–continuum transitions give rise to a negative delay that approaches zero in the limit of high photoelectron energy [19–21]. Hence, the total atomic delay depends on the target system, state and photon energy. If altogether neglected, these effects can lead for already available 100 as pulses to errors in the reconstructed pulse duration of 10%.

Corrections to the FROG-CRAB and PROOF methods have been proposed [22], and, for noble gas atoms, detailed target-dependent atomic delays have been computed [23–26]. Still, uncertainties remain regarding the discrepancy between experiment and theory. A new method that could measure the properties of attosecond pulses independent of the complex atomic response would improve the accuracy of attosecond pulse characterization and open up for new types of precision experiments.

In this article, we propose a new scheme to measure the spectral phase of attosecond pulses by ionization of a bound electron wave packet. The key points are that: (i) the pump and probe steps are *sequential*, (ii) the intermediate states are *bound* and (iii) the photoelectron is measured over *all detection angles*. As we will demonstrate, these three points result in an elimination of the dependence on dipole phases.

The elimination is exact provided that the parent cation is spherically symmetric and that correlation effects are negligible. Using Rydberg states as intermediate states is advantageous as they have single-particle character and possess little correlation. Photoionization cross sections are, however, small leading to weaker signal strengths. Alkali atoms would be ideal because they fulfill perfectly the spherical symmetry condition. In addition, the preparation of Rydberg wave packets can be performed using optical laser pulses.Noble gases are also a possibility, even though the ionic state is generally not spherically symmetric and excitation energies are in the

* stefan.pabst@cfa.harvard.edu
† marcus.dahlstrom@fysik.su.se

UV regime making it less favorable.

We will also show that multi-level wave packets are useful for analysis of pulses with complex spectral structure and that they allow for intrinsic self-consistency checks for the retrieved phases.

Rydberg states have been exploited before in attosecond experiments, but mainly with the focus on characterizing the bound electronic wave packet and not to characterize UV pulses [27, 28]. Another source of inspiration for our method is the recent work by You, Rohringer and Dahlström, where it was proposed that non-sequential two-photon hole transitions can be used as an alternative method for attosecond pulse characterization [29]. Nonetheless, we will demonstrate many advantages of sequential laser excitation using multiple electronic bound states as intermediate states.

In Sec. II, we discuss the theory behind our proposed method. In Sec. III A, we show examples how to reconstruct the spectral phase of an isolated attosecond pulse and an attosecond pulse train by using a Rydberg wave packet in potassium. The influence of electronic correlation effects are discussed in Sec. III B. We show that the dipole phase dependence due to inner-shell correlations and Fano resonances is much smaller in the angle-integrated photoelectron spectrum than in the directional photoelectron spectrum. Atomic units are used: $\hbar = |e| = 4\pi\epsilon_0 = 1$ unless otherwise stated.

## II. THEORY

### A. The basic idea

In this article we propose a scheme for UV pulse characterization that relies on photoionization of an electron wave packet for direct interference of different UV components. The basic idea is illustrated in Fig. 1.

Step 1 is preparation (pump) of a coherent electron wave packet

$$|\psi(t)\rangle = \sum_j c_j\, e^{-i\epsilon_j t}\, |j\rangle, \tag{1}$$

where $\epsilon_j$ and $c_j$ are the energy and complex amplitude of state $j$, respectively. The details of the preparation of the bound wave packet are not important. However, the pump process must be completed before the attosecond pulse starts the ionization process (probe), so that pump and probe steps are sequential. For characterization of the UV pulse it is important that the wave packet states have the same parity (in more detail the wave packet states must be able to reach the same final state via one-photon absorption). Populated states with opposite parity, such as a partially depleted initial state, will not interfere with photoelectrons from the wave packet when detection in all angles is assumed. Preparation of wave packet states with the same parity as the ground state allows for interference of UV components that are several eV apart and may be useful in special cases. However, we will focus on wave packets with opposite parity to the initial state.

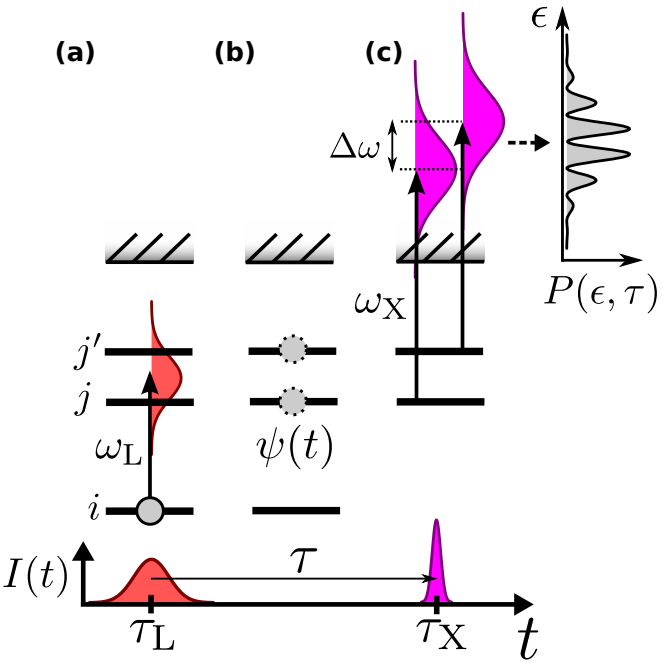


FIG. 1. Sketch of the method to characterize an UV pulse using a bound electron wave packet. (a) Preparation of the wave packet with laser pulse. (b) Field-free propagation of the electronic wave packet $\psi$ for the duration $\tau$. (c) Ionization of the wave packet by the UV pulse. Due to the coherent superposition of different electronic states, different spectral components of the UV pulse are absorbed to reach the same final continuum state with energy $\epsilon$. The interferences between the different spectral components contain the spectral phase information of the UV pulse that can be extracted by varying the delay $\tau$ and repeating the experiment.

Step 2 is field-free propagation of the wave packet for a time duration $\tau$. In step 3, the UV pulse arrives at the target,

$$E_X(\omega,\tau) = |E_X(\omega)|\, e^{i\omega\tau + i\phi_X(\omega)}, \tag{2}$$

and ionizes the wave packet, as illustrated in Fig. 1. $|E_X(\omega)|$ and $\phi_X(\omega)$ are the amplitude and phase of the unshifted UV pulse, namely for $\tau = 0$. In the time domain the electric field is given by

$$\tilde{E}_X(t,\tau) = \frac{1}{2\pi}\int d\omega\; E_X(\omega)\, e^{-i\omega(t-\tau)+i\phi_X(\omega)} = \tilde{E}_X(t-\tau,0), \tag{3}$$

which shows that a pulse with a given $\tau$ corresponds to an unshifted pulse delayed by $\tau$. As step 3 is a one-photon ionization process, the photoelectron amplitude is given by first-order perturbation theory,

$$\begin{aligned} c_f(\tau) &= \lim_{t'\to\infty} \frac{1}{i}\sum_j c_j\, d_{fj} \int^{t'} dt\; \tilde{E}_X(t,\tau)\, e^{i\omega_{fj}t} \\ &= -i\sum_j c_j\, d_{fj}\, |E_X(\omega_{fj})|\, e^{i\omega_{fj}\tau + i\phi_X(\omega_{fj})}, \end{aligned} \tag{4}$$

where $d_{fj}$ is the dipole transition moment from the bound state $|j\rangle$ to the continuum state $|f\rangle$. The lower bound of the time integral can be set to $-\infty$ because the ionization step of the wave packet is sequential and the $c_j$ amplitudes can be treated as constants.

The jitter between the pump and the probe pulses may lead to phase uncertainties. However, Rydberg states in alkali atoms can be pumped with IR pulses that are phase-locked to the UV field through the IR-driven high-order harmonic generation process. In this case jitter is removed as efficiently as for the FROG-CRAB and PROOF methods.

Different UV energies, $\omega_{fj} = \epsilon_f - \epsilon_j$, are required to reach the same final state from different bound states of wave packet, as shown in Fig. 1(c). The interference of the different ionization pathways make it possible to learn about the phase relation between the different spectral components of the UV pulse. The final photoelectron spectrum reads

$$P(\mathbf{k}_f,\tau) = |c_f(\tau)|^2 = \sum_j \left( A_j + \sum_{j'>j} B_{jj'} \cos\Theta_{jj'} \right), \quad (5)$$

where $\mathbf{k}_f$ is the momentum of the photoelectron with energy $\epsilon_f = k_f/2$. The variable $A_j$ is the isolated contribution from the wave packet state $|j\rangle$ to $|f\rangle$, while $B_{jj'}$ and $\Theta_{jj'}$ are the amplitude and phase of quantum interference between different parts of the wave packet with energies $\epsilon_{j'} > \epsilon_j$. The explicit form of the coefficients in Eq. (4) are

$$A_j = |c_j|^2\,|d_{fj}|^2\,|E_{\mathrm{X}}(\omega_{fj})|^2, \quad (6a)$$
$$B_{jj'} = 2\,|c_j\,c_{j'}|\;|d_{fj}\,d_{fj'}|\;|E_{\mathrm{X}}(\omega_{fj})E_{\mathrm{X}}(\omega_{fj'})| \quad (6b)$$
$$\Theta_{jj'} = \arg\!\left[c_j\,c_{j'}^*\;d_{fj}\,d_{fj'}^*\;E_{\mathrm{X}}(\omega_{fj},\tau)\,E_{\mathrm{X}}^*(\omega_{fj'},\tau)\right]. \quad (6c)$$

The phase of the interference pattern can be rewritten to clearly show the quantum beating of the probability, at each energy difference $\omega_{j'j} = \omega_{fj} - \omega_{fj'} > 0$, as

$$\Theta_{jj'} = \omega_{j'j}\,\tau + \phi_X^{(jj')}(\epsilon_f) + \phi_D^{(jj')}(\epsilon_f) + \phi_I^{(jj')}, \quad (7)$$

where the phase differences read

$$\phi_X^{(jj')}(\epsilon_f) = \phi_{\mathrm{X}}(\omega_{fj}) - \phi_{\mathrm{X}}(\omega_{fj'}) \approx \tau_{\mathrm{X}}^{(\mathrm{GD})}(\bar{\omega}_{jj'}^{(f)})\;\omega_{j'j}, \quad (8a)$$
$$\phi_D^{(jj')}(\epsilon_f) = \arg[d_{fj}] - \arg[d_{fj'}], \quad (8b)$$
$$\phi_I^{(jj')} = \arg[c_j] - \arg[c_{j'}]. \quad (8c)$$

Eq. (8a) defines the group delay $\tau_{\mathrm{X}}^{(\mathrm{GD})}(\bar{\omega}_{jj'}^{(f)})$ of the UV pulse computed as a finite-difference derivative at the mean photon energy, $\bar{\omega}_{jj'}^{(f)} = (\omega_{fj} + \omega_{fj'})/2$. The dipole transition elements $d_{fj}$ are complex valued functions that contribute energy-dependent dipole phases to the phase difference $\phi_D^{(jj')}(\epsilon_f)$ in Eq. (8b). In contrast, $\phi_I^{(jj')}$ in Eq. (8c) is inherent to the preparation process of the bound wave packet and independent of the final photoelectron energy.

The main goal in characterizing the UV pulse is the determination of $\tau_{\mathrm{X}}^{(\mathrm{GD})}(\omega)$. If this group delay is known then the spectral phase $\phi_X(\omega)$ can be fully reconstructed (up to an absolute value) by numerical integration. However, the oscillations in the photoelectron spectrum depend also on $\phi_I^{(jj')}$ and $\phi_D^{(jj')}(\epsilon_f)$. The intrinsic phase shift $\phi_I^{(jj')}$ does not present an obstacle as it is energy independent and corresponds to a constant shift of the pump-probe delay by $\phi_I^{(jj')}/\omega_{j'j}$. However, the energy dependence of the dipole phases $\phi_D^{(jj')}(\epsilon_f)$ may prevent accurate determination of the group delay of the UV pulse.

Before we continue our discussion, we discuss the importance of higher-order effects that go beyond first-order perturbation [cf. Eq (4)]. Pazourek *et al.* [28] have pointed out that depopulation of the initial states results in an additional universal energy-dependent phase contribution in Eq. (7) that varies by multiple of $\pi$ across the pulse spectrum. This is particularly an issue when the probability of ionization is high. By using Rydberg states, we reduce this phase dependence to a minimum as UV pulses are weak and cross sections of Rydberg states are two or more orders of magnitude smaller than for bound states. In Sec. III A, we give explicit number for this effect and show that it is indeed negligible.

Similarly, a differential AC Stark shift between the Rydberg states due to the ionizing UV pulse is a third-order effect and can lead to phase corrections. Furthermore, the AC Stark shifts of neighboring Rydberg at UV frequencies become more similar and approach quickly the ponderomotive potential, $U_p = E^2/(4\omega^2)$, as the principle quantum number $n$ increases. For an $10^{12}$ W/cm$^2$ pulse with $\omega = 50$ eV, the ponderomotive potential is less than 0.1 meV and the differential AC Stark shift between Rydberg states is even smaller allowing us to safely neglect AC Stark effects.

### B. Uncorrelated spherically symmetric systems

For spherically symmetric systems, and more specifically for spherically symmetric cations without correlation effects, the radial dipole moment to any energy eigenstate (continuum or bound) can be chosen to be real [30]. As a result, the angle-integrated photoelectron spectrum does not have an energy-dependent $\phi_D^{(jj')}$-phase anymore. To see this, we start with a partial wave expansion of the final momentum state,

$$\psi_{\mathbf{k}}^-(\mathbf{r}) = \frac{1}{k^{1/2}} \sum_{L=0}^{\infty} \sum_{M=-L}^{L} i^L e^{-i\eta_L} Y_{LM}^*(\hat{\mathbf{k}})\,Y_{LM}(\hat{\mathbf{r}})\,R_{\epsilon L}(r), \quad (9)$$

where $\mathbf{k} = k\,\hat{\mathbf{k}}$ is the momentum of the photoelectron and its energy is given by $\epsilon_f = k^2/2$ [31]. Note that $\psi_{\mathbf{k}}^-$

is momentum normalized, $\langle\, \psi^-_{\mathbf{k}} \,|\, \psi^-_{\mathbf{k}'} \,\rangle = \delta(\mathbf{k}-\mathbf{k}')$, while the real radial wave functions are chosen to be energy normalized, $\langle\, R_{\epsilon L} \,|\, R_{\epsilon' L} \,\rangle = \delta(\epsilon-\epsilon')$. Inserting Eq. (9) for the final state, $f$, in Eq. (4) leads to the following expression for the photoelectron spectrum,

$$\begin{aligned} P(\mathbf{k},\tau) &= |c_{\mathbf{k}}(\tau)|^2 \qquad (10)\\ &= \frac{1}{k}\sum_j\sum_{j'} c_j c^*_{j'} \sum_{L,M}\sum_{L',M'} i^{L-L'}\, Y_{L'M'}(\hat{\mathbf{k}})\, Y^*_{LM}(\hat{\mathbf{k}}) \\ &\quad\times e^{-i\eta_L + i\eta_{L'}}\; d_{fj}\, d^*_{f'j'}\; E_{\mathrm{X}}(\omega_{fj},\tau)\, E^*_{\mathrm{X}}(\omega_{fj'},\tau), \end{aligned}$$

where we used the partial-wave basis $|f\rangle = |\epsilon_f LM\rangle$ and $d_{fj} = \langle f|\hat{d}|j\rangle = \langle \epsilon_f L\|r\|n_j L_j\rangle\; C^{LM}_{L_j M_j;1\mu}\sqrt{2L+1}^{-1}$ with $\mu$ being the polarization of the ionizing UV pulse. In Eq. (10) the sums on $j$ and $j'$ run over all excited states of the prepared wave packet. Since the radial part of the continuum states and the bound state are chosen to be real functions, the reduced matrix element, $\langle \epsilon_f L\|r\|n_j L_j\rangle$, and the dipole, $d_{fj}$, are real and do not contribute to a phase difference in the photoelectron spectrum.

However, Eq. (10) depends on the scattering phase differences between all final partial waves states resulting in non-trivial angle and energy dependencies. By performing an angle-integrated measurement, the dependencies on the dipole phase can be eliminated,

$$\begin{aligned} P(\epsilon,\tau) &= \int d\Omega_{\mathbf{k}}\; |c_{\mathbf{k}}(\tau)|^2 \qquad (11)\\ &= \sum_{L_f,j',j} c_j c^*_{j'} d_{fj} d_{fj'}\; E_{\mathrm{X}}(\omega_{fj},\tau) E^*_{\mathrm{X}}(\omega_{fj'},\tau), \end{aligned}$$

where the orthogonality of spherical harmonics reduces for each $(j,j')$ pair to a sum over all final angular momenta $L_f$. Rewriting Eq. (11) by grouping contributions form the same $(j = j')$ and different electronic states $(j \neq j')$ together, we obtain

$$P(\epsilon,\tau) = \sum_j \left( \bar{A}_j + \sum_{j'>j} \bar{B}_{jj'} \cos\bar{\Theta}_{jj'} \right) \qquad (12)$$

where the variables read

$$\bar{A}_j = \sum_{L_f} |c_j|^2\; |d_{fj}|^2\; |E_{\mathrm{X}}(\omega_{fj})|^2/k, \qquad (13a)$$

$$\bar{B}_{jj'}, = \sum_{L_f} d_{fj} d_{fj'}\; |c_j c_{j'}|\; |E_{\mathrm{X}}(\omega_{fj})\, E_{\mathrm{X}}(\omega_{fj'})|/k, \qquad (13b)$$

$$\bar{\Theta}_{jj'} = \omega_{j'j}\,\tau + \phi_X^{(jj')}(\epsilon_f) + \phi_I^{(jj')}, \qquad (13c)$$

where we write the index $f$ explicitly on $L_f$ for clarity. The phase term, $\Theta_{jj'}$, is independent of atomic scattering (or dipole) phases and of $L_f$. As the dipoles can be positive or negative, there should be no absolute magnitude around $d_{fj}d_{fj'}$ in Eq. (13b). Consequently, the phase modulation depends on the properties of the wave packet preparation, $\phi_I^{(jj')}$ and on the phases of the UV field, $\phi_X^{(jj')}(\epsilon_f)$, but not on the final scattering phases $\eta_{L_f}(k)$ — exactly what we wanted.

When $N$ states are involved in the electron wave packet, $\psi(t)$, we obtain $\binom{N}{2}$ different $\omega_{jj'}$ oscillations with their corresponding phase differences $\phi_X^{(j_1 j_2)}$. It turns out there exist groups of three phase differences that obey the relation

$$\begin{aligned} \phi_X^{(j_1 j_3)}(\epsilon_f) &= \phi_X(\omega_{fj_1}) - \phi_X(\omega_{fj_3}) \qquad (14)\\ &= \phi_X(\omega_{fj_1}) - \phi_X(\omega_{fj_2}) + \phi_X(\omega_{fj_2}) - \phi_X(\omega_{fj_3}) \\ &= \phi_X^{(j_1 j_2)}(\epsilon_f) + \phi_X^{(j_2 j_3)}(\epsilon_f). \end{aligned}$$

Eq. (14) holds also true for the retrieved phase differences, $\phi_X^{(jj')}(\epsilon_f) + \phi_I^{(jj')}$, up to a constant, because $\phi_I^{(j_1 j_2)}$ does not need to fulfill any special relation. This connection can be used to cross-reference the extracted phases and to check the consistency of the retrieved phases. To our knowledge, no other ultrafast pulse reconstruction method (for femtosecond or attosecond pulses) possess such a feature.

Our scheme to characterize UV pulses has several advantages that can be summarized as follows:

- Angle-integrated detection increases the total signal and ensures that ionization pathways to different final angular momenta of the photoelectron do not affect the phase reconstruction.
- Rydberg states make it possible to probe spectral phase differences bridging small energy distances as the energy difference between Rydberg states goes like $n^{-3}$.
- A combination of small *and* large energy differences, $\omega_{j'j}$, makes it possible to probe phase differences between close-by and distance spectral phase components. This is especially useful if certain spectral regions have negligible intensity and need to be bridged, as is the case for pulse trains.
- There is no constraint on the polarization of the UV pulse. It works for linearly, circularly, and elliptically polarized pulses.
- Wave packets with $N$ electron states (with the same angular momentum) leads to $\binom{N}{2}$ beating frequencies in the photoelectron spectrum providing redundant information [Eq. (14)] to cross-check the consistency of the reconstruction.

In more detail, electron correlation results in complex-valued dipole moments that may affect the pulse reconstruction, even if photoelectron is detected over all angles. As we will show in Sec. III B for the case of Rydberg wave packets, these effects are surprisingly small even in correlated energy regions close to autoionizing resonances.

## III. RESULTS

In this section, we first use Rydberg wave packets to characterize a single attosecond pulse (Secs. III A 1

and III A 2) and an attosecond pulse train (Sec. III A 3). We then use photoionization of Rydberg wave packets to study electronic structure properties of angle-resolved photoelectrons (Sec. III B 1). Finally, we study the influence of electron correlation in the case of potassium in a resonance free region (Sec. III B 1) and in neon near the $2s^{-1}3s$ Fano resonance (Sec. III B 4).

We choose potassium as our main system of interest. Atomic alkali metals possess several advantages and have been used for ultrafast experiments [32, 33]: (1) After removal of the the outermost $s$ electron, alkali cations are closed-shell systems with relatively small amount of correlation. (2) The mean-field potential of alkali cations is spherically symmetric fulfilling exactly the conditions for real reduced dipole matrix elements. (3) The excitation energies of the Rydberg states in all alkali metals lie within 1.4 eV and 5.4 eV [34]. This is a convenient energy range as it is easily accessible with common laser systems and standard nonlinear optics that make it possible to transfer up to 100% of the population into Rydberg states.

A practical question that arises when using Rydberg states is the signal strength because Rydberg states have much lower photoionization cross sections ($\propto n^{-3}$) than valence shells [35]. To characterize attosecond pulses, low-lying Rydberg state with $n < 10$ are sufficient. Their cross section is roughly 100 times weaker than the outermost valence shell. Given common gas parameters ($10^{17}$ atoms/cm$^3$, 1 mm gas jet diameter [36]) and attosecond pulse parameters ($10^{11}$ photons/s, 1 kHz–1 MHz repetition rate [4]), we estimate a total number of $10^3$–$10^6$ electrons/s to get ionized for photon energies up to 100 eV.

Dipole-dipole interactions between Rydberg states can lead to corrections to the energy level and the Rydberg wavefunction. The energy corrections are on the 1 meV scale for the Rydberg states considered here ($n < 10$) and gas densities up to $10^{17}$ atoms/cm$^3$. Rydberg states up to $n < 10$ have periods in the tens of femtosecond regime, which are hundred times faster than the picosecond-scale corrections corresponding to 1 meV changes. Consequently, the interaction between Rydberg states or neighboring atoms is negligible for this type of measurement.

All results obtained by explicit time propagation [37] utilize the XCID program [38] with the following numerical parameters [39] and the wavefunction splitting method to analyze the photoelectron spectrum as described in Ref. [40]. This method has been successfully used to analyze photoelectron spectra in the multiphoton regime [41, 42]. In this work we are staying in the one-photon regime. Correlation effects for potassium are studies by means of the random phase approximation with exchange (RPAE) by adapting existing numerical codes [43] with the initial state being a given $np$ virtual orbital obtained by the Hartree-Fock (HF) equation of the $K^+$ core [44, 45]. TDCIS is also used to study correlation effects in neon, as it has been shown to describe well many-body physics in the attosecond [46] and strong-field regime [47].

## A. Pulse characterization

### 1. *Single Pulse + 2-level wave packet*

As Rydberg wave packets can be easily prepared with common laser systems, we omit the description of its preparation. In our first example, we choose the wave packet in potassium (K) to be a coherent superposition between the $3p^6 4p$ and $3p^6 5p$ Rydberg states,

$$|\Psi(t)\rangle = \frac{1}{\sqrt{2}} \sum_{n=4,5} e^{-i\,\varepsilon_{np}\,t}\,|np\rangle. \tag{15}$$

We omit reference to the inner-shell configuration as we are only interested in the Rydberg electron and assume that the ionic configuration will not change (see Sec. III B 4 for a more general discussion and the influence of interchannel coupling). Potassium is treated within the HF level, where the HF procedure is done for $K^+$. The valence electron interacts with a mean-field potential of $K^+$ and interchannel correlation is neglected.

In the probe step, the $4p$–$5p$ Rydberg wave packet is ionized by the attosecond pulse. We consider an isolated attosecond pulse with constant spectral phase: $\phi_X(\omega) = 0$, with a quadratic spectral phase: $\phi_X(\omega) = 100\ (\omega-\omega_0)^2$ and with a cubic spectral phase: $\phi_X(\omega) = 100\ (\omega-\omega_0)^3$. Each attosecond pulse has a central photon energy of $\omega_0 = 74$ eV ($= 2.72$ a.u.) and a full-width-half-maximum (FWHM) spectral intensity width of 7.4 eV ($= 0.27$ a.u.) corresponding to a pulse duration of 247 as for a Fourier-limited pulse. The pulse with linear chirp (quadratic phase) is symmetrically stretched in time increasing the pulse duration, while the pulse with quadratic chirp (third-order phase) experiences an asymmetric pulse deformation.

In Figs. 2(a-c) the photoelectron spectra, $P(\epsilon,\tau)$, are shown for the attosecond pulse with (a) no chirp, (b) linear chirp and (c) quadratic chirp. In accordance with Eqs. (8a) and (13c), the chirps are directly visible as a constant, linear and quadratic shift of the beating patterns in Figs. 2(a-c), respectively.

In Figs. 2(d-f) the photoelectron spectra, $P(\epsilon,\nu)$, are shown where the delay axis is Fourier transformed. In all three cases a static signal and an oscillating signal with the beating frequency corresponding to $\epsilon_{5p}-\epsilon_{4p} = 1.36$ eV is visible. The discreteness in the data is defined by the the length of the delay range used in the calculations, which is 500 a.u. (12.1 fs).

In Figs. 2(g-i) the retrieved phases of the 1.36 eV beating signal for the different attosecond pulses are shown. According to Eq. (13c), these phase differences correspond to $\phi_X^{(jj')}(\epsilon_f) + \phi_I^{(jj')}$, where $j = 4p$ and $j' = 5p$. The intrinsic phases of the Rydberg wave packet $\phi_I^{(jj')}$ are subtracted in Figs. 2(g-i) such that the retrieved phase at the spectral peak of the beating signal is 0. The phase $\phi_I^{(jj')}$ does not affect the reconstruction of the spectral chirp of the pulse (see Sec. II). The analytic solutions of the phase differences, $\phi_X^{jj'}(\epsilon_f)$, are plotted as

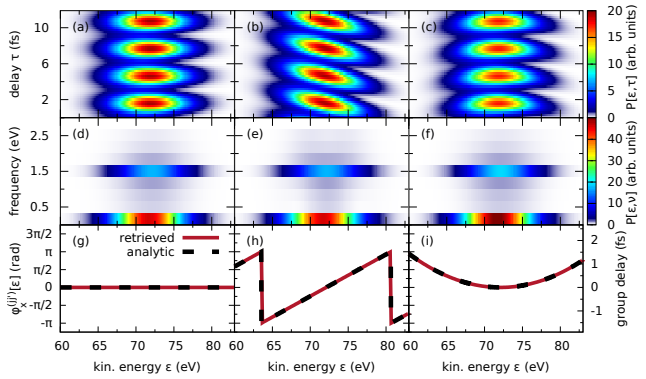


FIG. 2. (a-c) Photoelectron spectra of the $4p$–$5p$ Rydberg wave packet ionized by an attosecond pulse with (a) no chirp, (b) a linear chirp, and (c) a quadratic chirp ionizing as a function of the pulse delay. (d-f) Photoelectron spectra where the delay axis is Fourier transformed. The spectrum contains a static signal and an oscillating component with frequency 1.36 eV. (g-i) Retrieved phase differences of the 1.36 eV component. Analytic results are shown as black dashed lines. The corresponding group delay of the phase differences is shown on the right.

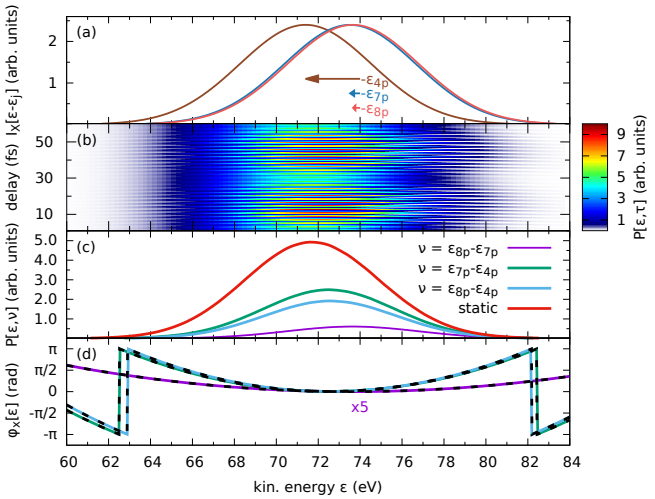


FIG. 3. (a) Spectra of the attosecond pulse, $E_X(\omega_{fj})$, shifted by the Rydberg binding energies $\epsilon_{4p}, \epsilon_{7p}$, and $\epsilon_{8p}$ (indicated by arrows). (b) Photoelectron spectrum of the $4p$–$7p$–$8p$ Rydberg wave packet ionized by a quadratic-chirped single attosecond pulse. (c) The static and the 0.14 eV, 2.12 eV, and 2.26 eV oscillating signals of the photoelectron spectrum. (d) Retrieved phases of the three frequency components. The analytic results are shown as black dashed lines.

black-dashed lines, and agree perfectly with the retrieved phases.

### 2. *Single Pulse + multi-level wave packet*

The Rydberg wave packet is not limited to be a superposition of two Rydberg states for characterization of UV pulses. Involving $N > 2$ states (with the same angular momentum $l$) in the Rydberg wave packet is even more beneficial as $\binom{N}{2}$ beating frequencies occur in the photoelectron spectra—all containing spectral information about the pulse.

We consider the 3-level Rydberg wave packet,

$$|\Psi(t)\rangle = \frac{1}{\sqrt{3}} \sum_{n=4,7,8} e^{-i\,\varepsilon_{np}\,(t-t_0)}\,|np\rangle, \qquad (16)$$

which provides two high frequency beatings, $\omega_{84} = \epsilon_{8p} - \epsilon_{4p} = 2.26$ eV and $\omega_{74} = \epsilon_{7p} - \epsilon_{4p} = 2.12$ eV, and one low frequency beating $\omega_{87} = \epsilon_{8p} - \epsilon_{7p} = 0.14$ eV. The reference time, where all phases of the wave packet are the same, is arbitrarily chosen to be $t_0 = -600$ a.u. In Fig. 3(a), the pulse spectrum shifted by the ionization potentials is shown to indicate where the corresponding photoelectron distributions are expected.

Fig. 3(b) shows the photoelectron spectrum, $P(\epsilon,\tau)$, for ionization of the 3-level Rydberg wave packet with the quadratic chirped pulse from Sec. III A 1. The photoelectron spectra, $P(\epsilon,\nu)$, for the three frequencies $\nu = \omega_{47}, \omega_{48}, \omega_{78}$ are shown in Fig. 3(c).

The retrieved phases and the analytic result match perfectly for the three beating patterns [see Fig. 3(d)]. All three curves are parabolas with curvatures $3\beta\omega_{j'j}$ depending on the quadratic chirp, $\beta = 100$, and on the energy difference between the states, $\omega_{j'j}$. Also the relations between $\phi_X^{(jj')}$ [see Eq. (14)] hold for all combinations. This demonstrates that our method provides an internal mechanism to confirm the consistency of the retrieved phases.

### 3. *Pulse train + multi-level wave packet*

We will now demonstrate that the $4p$–$7p$–$8p$ three-level Rydberg wave packet from Sec. III A 2 can be applied to probe the phase of pulse trains on the attosecond and femtosecond time scales simultaneously. We choose a pulse train that consists of the 48$^{\text{th}}$, 49$^{\text{th}}$ and 50$^{\text{th}}$ harmonic of 800 nm with some rather complicated phase relations: The 48$^{\text{th}}$ harmonic has no spectral chirp but a phase constant of $\pi/4$. The 49$^{\text{th}}$ harmonic has a linear chirp, $\phi_X(\omega) = -0.5/\delta\omega^2(\omega - \nu_{55})^2$. Finally, the 50$^{\text{th}}$ harmonic has a quadratic chirp, $\phi_X(\omega) = 0.5/\delta\omega^3(\omega - \nu_{56})^3 + \pi/3$. Each harmonic has a spectral intensity FWHM width of $\delta\omega = 400$ meV.

The 3-level Rydberg wave packet allows for interference of spectral components within an individual harmonic and between adjacent harmonics. This is visualized in Fig. 4(a) where the UV spectrum is shifted by the three different binding energies. The energy difference $\omega_{7p,8p}$ is smaller than the spectral width of the harmonics and it, therefore, allows for probing the phase relation

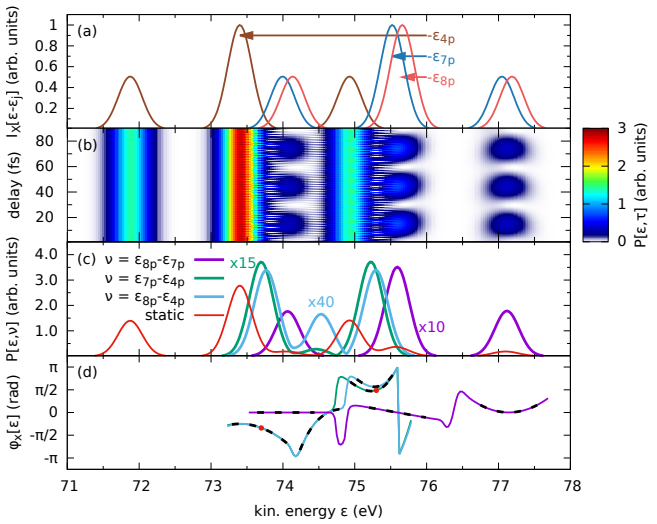


FIG. 4. (a) Spectra of the attosecond pulse train, $E_{\mathrm{X}}(\omega_{fj})$, shifted by the Rydberg binding energies $\epsilon_{4p}, \epsilon_{7p}$, and $\epsilon_{8p}$ (indicated by arrows). (b) Photoelectron spectrum of the $4p$–$7p$–$8p$ Rydberg wave packet ionized by the attosecond pulse train. (c) The static and the 0.14 eV, 2.12 eV, and 2.26 eV oscillating components of the photoelectron spectrum. (d) Retrieved phases of the three frequency components. The analytic results are shown as black dashed lines. The highlighted phases (red circles) at 73.7 eV and 75.3 eV for the $4p$–$7p$ beating are used to determined the relative phases between harmonics.

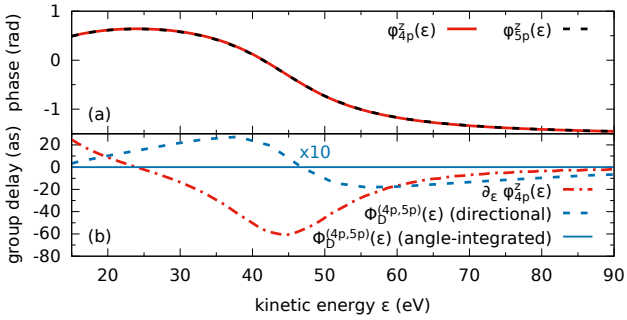


FIG. 5. (a) Dipole phases $\varphi^z_{4p/5p}(\epsilon) = \arg[\langle \epsilon, \vec{e}_z|z|4p/5p\rangle]$ for ionizing an electron in $z$-direction with kinetic energy $\epsilon$. (b) Delay of the directional dipole phase $\varphi^z_{4p}(\epsilon)$ (red dashed line) and the relative delay between $4p$ and $5p$, $\phi_D^{(4p,5p)}(\epsilon)$, entering the directional (blue dashed line) and angle-integrated (blue solid line) photoelectron spectra. Data is produced by static HF calculations.

within each harmonic individually [by overlap of red and blue in Fig. 4(a)]. The energy differences $\omega_{74}$ and $\omega_{84}$ are comparable to the spectral separation between harmonics and allow for probing of the phase relation between adjacent harmonics [by overlap of the brown curve with the blue or red curves in Fig. 4(a)].

Figure 4(b) shows the photoelectron spectrum $P(\epsilon, \tau)$ from the 3-level Rydberg wave packet ionized by the attosecond pulse train. The three main delay-independent peaks correspond to the ionization of the $4p$ electron by the three harmonics. The contributions of $7p$ and $8p$ cannot be spectrally distinguished, but their interference results in three distinct low-frequency beatings in Fig. 4(b).

The $\omega_{4p,7p}$ and $\omega_{4p,8p}$ modulations are located at kinetic energies 73.7 eV and 75.3 eV in Fig. 4(b), corresponding to interference of harmonic 48 with 49 and harmonic 49 with 50, respectively. The extracted phases from all three modulations, shown in Fig. 4(d), agree perfectly with the analytic predictions and Eq. (14) hold for kinetic energies where all three beating patterns have a non-vanishing signal. In this way, we can reconstruct the phase within each harmonic (up to a constant) using the $7p$–$8p$ beating signal. This shown by the violet curve in Fig. 4(d), which displays that harmonic 48 has no chirp, harmonic 49 has a linear chirp while harmonic 50 has a quadratic chirp. To determine the phase between two neighboring harmonics, the phase at one specific kinetic energy of the $4p$–$7p$ or $4p$–$8p$ oscillations needs to be found. At 73.7 eV and 75.3 eV, the phase differences of the $4p$–$7p$ modulation are $-0.34\pi$ and $0.49\pi$, respectively [red dot markings in Fig. 4(d)]. Using our knowledge about the spectral phase within each harmonics, which we just determined, we find that the constant phase difference between harmonic 48 and 49 is $-\pi/4$, and between harmonic 49 and 50 is $\pi/3$. Hence, we have fully reconstructed the spectral phases of the pulse train up to a constant global phase. This shows that our method is useful for characterization of pulse trains (on both attosecond and femtosecond time scales) and that it can be used to benchmark the accuracy of the RABBITT-method [3].

### B. Electronic structure

#### 1. *Directional dipole phases*

As we discussed in Sec. II and showed in Sec. III A, the dipole phase drops out when studying the angle-integrated photoelectron spectrum. In this section, we analyze the dipole phase dependence of the directional photoelectron spectrum for an electron ionized along the field polarization $\hat{\mathbf{z}}$.

In Fig. 5(a) we show the dipole phases $\varphi^z_{4p/5p}(\epsilon) = \arg[\langle \epsilon, \hat{\mathbf{z}}|z|4p/5p\rangle]$ for ionization of an electron in $\hat{\mathbf{z}}$-direction with kinetic energy $\epsilon$. The dipole phases vary non-monotonically by $\pi/2$ over an energy region from 20–90 eV. This behavior can be attributed to a Cooper minimum in the photoionization cross-section of K from the $np$ states. The dipole phase of the Rydberg states $4p$ and $5p$ of K are almost exactly the same. What enters in our scheme is the phase differences between the two dipoles phases.

In Fig. 5(b), we compare the delay due to the dipole phase difference of $4p$ and $5p$, $\phi_D^{(j,j')}(\epsilon)/\omega_{j'j} = [\varphi^z_{4p}(\epsilon) - \varphi^z_{5p}(\epsilon)]/(\epsilon_{5p} - \epsilon_{4p})$, that enters in our proposed method

(blue dashed line) with the Wigner delay, $\partial_\epsilon \phi_D^{(4p,5p)}(\epsilon)$, that enters in the FROG-CRAB, PROOF, and RABITT (red dotted-dashed line) [in addition to an IR-induced delay—not considered here]. The Wigner delay is an order of magnitude larger than the delay of our directed method. This shows that even without angle-integration, the influence of the dipole phase is strongly reduced thanks to the similarity between neighboring Rydberg states. The delay due to the angle-integrated phase difference, $\phi_D^{(4p,5p)}(\epsilon)$, is exactly zero (blue solid line), as expected from our discussion in Sec. II.

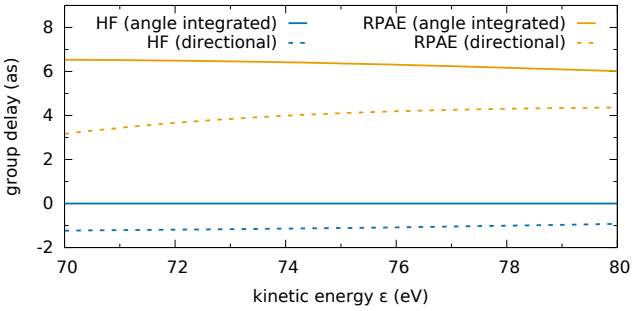


FIG. 6. Dipole-induced delay for the directional (dashed lines) and for the angle-integrated (solid lines) photoelectron spectra of potassium treated in the HF approximation (blue lines) and RPAE (yellow lines).

### 2. *Critical pulse duration*

The curvature (second spectral derivative) of the dipole phase is important for the pulse characterization because it leads an energy dependent Wigner delay and, thus, artificial deformations in the reconstructed pulse. The curvature is around 3 as/eV for directed photoelectrons at photon energies up to 50 eV in potassium from 4p or 5p (a value that is reasonable to assume also for noble gas atoms). Given a Gaussian Fourier-limited pulse with FWHM-pulse duration $\delta t$, a constant dipole phase curvature $c$, implies that the reconstructed phase becomes $\phi = \frac{c}{2}(\omega - \omega_0)^2$ (plus unknown constant). The reconstructed FWHM-pulse duration becomes

$$\delta t_{\text{recon}} = \delta t \sqrt{1 + 16\,\ln^2(2)\; c^2/\delta t^4} \quad = \delta t \sqrt{1 + (\delta t_{\text{crit}}/\delta t)^4}, \tag{17}$$

where we have defined a critical pulse duration, $\delta t_{\text{crit}} = \sqrt{4\ln(2)\,c}$. Expressed in commonly used units, the critical pulse duration is: $\tau_{\text{crit}}[\text{as}] = 42.7\sqrt{c[\text{as/eV}]}$.

If we use $c \sim 3$ as/eV, the critical pulse duration is 74 as. This shows that not just for the characterization of the shortest attosecond pulses or zeptosecond pulses [48, 49], the dipole phase cannot be ignored. Already for a 100 as Fourier-limited pulse the error is 14%. In our approach, the dipole phase curvature that enters (without angle-integration) is 40 times smaller, reducing the critical pulse duration to 11 as. With angle-integration, $c = 0$ and no critical duration exist.

As mentioned in Sec. II, depopulation introduces a universal energy dependent phase. The small cross sections and weak UV intensity lead to small depopulations and consequently to small phase effects. For K $4p$ ionized by an 100 as pulse ($10^{12}$ W/cm$^2$ peak intensity and 70 eV photon energy) leads to relative depopulation of $10^{-4}$ and a negligible depopulation-induced phase curvature of $c < 2 \times 10^{-4}$ as/eV.

Next, we estimate how much $c$ is affected by electron correlation effects.

### 3. *Residual correlation effects*

Once electronic correlations are considered, the dipole phase affects the photoelectron spectrum even after angle integration. Photoionization of alkali atoms is a prototypical test-case for correlation effects for close-to-threshold photoionization [50]. In this work we consider larger photon energies where, in general, correlation effects are expected to be smaller. In Fig. 6, we compare the retrieved phases of the $\omega_{4p,5p}$ oscillations of the directional (dashed lines) and angle-integrated (solid lines) photoelectron spectra of potassium treated within the Hartree-Fock approximation (HF; blue lines). This calculation builds on the perturbation diagram shown in Fig. 7 (a), where $j = 4p$, $5p$ are the excited Rydberg states and $f = ks$, $kd$ are the final photoelectron states, both computed within HF. This type of calculation contains no correlation effects by definition and the corresponding delay of the angle-integrated calculation is zero, as expected from Sec. II. In Fig. 6 we also show the random-phase approximation with exchange (RPAE; yellow lines), which includes additionally correlation effects with the electrons from the $Ar^+$ core $c = 3s$, $3p$, as illustrated by the perturbation diagrams in Fig. 7 (b)–(e). More details about RPAE are found in Ref. [45].

The direction of the photoelectron is chosen to be parallel to the laser polarization direction ($\theta = 0$). The energy range of 70–80 eV is chosen to avoid on-shell excitation of autoionizing resonances in the continuum (see Sec. III B 4) and to focus on the residual effect (virtual coupling) to other particle-hole excitations.

When correlation effects are included, the reduced dipole moments become complex-valued even in spherically symmetric systems resulting in a dipole phase dependence in the angle-integrated photoelectron spectrum. In Fig. 6, the RPAE results, which include correlation, show a weak energy dependence. The correlation induced delay in the angle-integrated spectrum (solid yellow line) is centered around 6 as. A constant delay difference is, however, not of interest and does not influence the determination of the spectral chirp. The energy de-

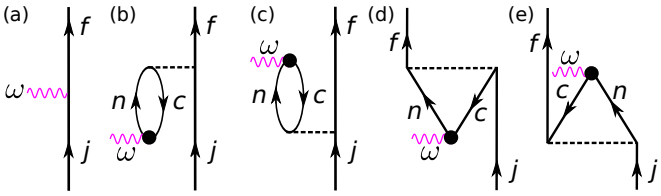


FIG. 7. Perturbation diagram for (a) HF, (b) direct-forward RPAE (c) direct-backward RPAE (d) exchange-forward RPAE and (e) exchange-backward RPAE. Up (down) arrows label electron (hole) states. Further details are given in the main text.

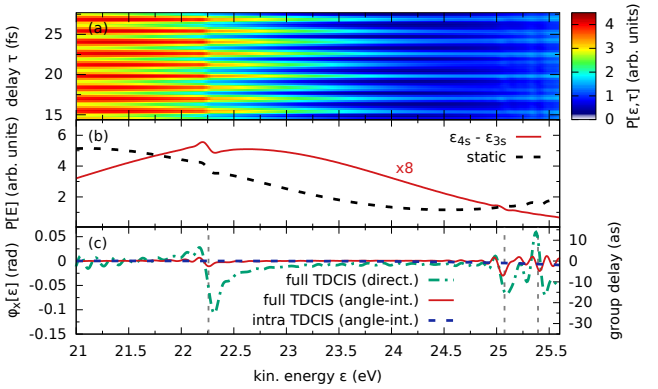


FIG. 8. (a) Angle-integrated photoelectron spectrum of the $2p^{-1}3s$–$2s^{-1}4s$ wave packet ionized by an isolated attosecond pulse. (b) The static (black dashed line) and the oscillating components (solid red line) of the angle-integrated photoelectron spectrum. (c) Retrieved phase of the oscillating components of the angle-integrated (red solid line) and directional (green dashed-dotted line) photoelectron spectrum for the full TDCIS model. The intrachannel TDCIS results for the angle-integrated photoelectron spectrum is shown as reference (blue dashed line). The corresponding group delay of the phase differences is shown on the right.

pendence is thanks to the Rydberg states again quite weak.

The average slope is -0.052 as/eV in the 70–80 eV range resulting in a critical pulse duration of $\tau_{\rm crit}$ = 9 as. The influence of correlation on the directional photoelectron (dashed yellow line) is with an average slope of 0.12 as/eV more than twice stronger than in the angle-integrated case. It shows also in the presence of correlations, the dipole phase dependency is reduced when studying the angle-integrated photoelectron spectrum.

The influence of correlation can be further reduced when going to higher Rydberg states, or when going to lighter atoms (e.g. sodium with neon-like core), which generally contain less electronic correlation.

#### 4. *Autoionizing resonances*

When the ionizing test pulse is resonant with autoionizing inner-shell excitations, Fano resonances become visible in the photoelectron spectrum, which are spectrally highly localized around the autoionizing resonance energy (in contrast to the residual effects discussed in Sec. III B 3). Since autoionization is a correlated process, the dipole phase dependence will survive in the photoelectron spectrum after angle integration in the form of amplitude and phase modulations in the beating patterns.

To demonstrate the influence of an autoionizing state, we choose neon and we target the lower $2s^{-1}ns$ autoionizing states, which are even-parity states and can only be reached with an even number of photons. First, we prepare a Rydberg wave packet between $2p^{-1}3s$ and $2p^{-1}4s$ with two 4.8 fs (= 200 a.u.) Gaussian pulses with center frequencies 16.8 eV and 19.7 eV. After the wave packet is prepared, we ionize it with a 508 as (= 21 a.u.) Fourier-limited Gaussian pulse with a center frequency of 25.9 eV (= 0.95 $E_h$), which ionizes the Rydberg electron but also drives the ionic transition between $2p^{-1}$ and $2s^{-1}$ leading to population of the autoionizing $2s^{-1}ns$ states. The calculations [51] are based on TDCIS, which accurately describes the $2s^{-1}np$ Fano resonances in neon [52].

Phase modulations in the beating pattern will only be due to $\phi_D^{jj'}(\epsilon_f)$ because $\Phi_X^{jj'}(\epsilon_f) = 0$ in Eq. (7). In Fig. 8(a), the angle-integrated photoelectron spectrum around the $2s^{-1}3s$ is shown and Fig. 8(b) shows the amplitude of the static and oscillating contributions. The $2s^{-1}3s$ and higher Fano-resonances are visible in the static and especially in the oscillating amplitudes. The static signal increases beyond 25 eV [see Fig. 8(b)] to two-photon absorption of the attosecond pulse. This process is not delay-dependent and contributes only to the static background.

The retrieved phases are shown in Fig. 8(c) where the energy position of the $2s^{-1}ns$ resonances are highlighted by vertical dashed lines. Also the intrachannel TDCIS result for the angle-integrated photoelectron spectrum is shown (blue dashed line), where the interchannel interactions are responsible for the autoionization of all $2s^{-1}nl$ states are not included. Ignoring interchannel effects eliminates correlation effects, and as a result no phase modulations around the resonance energies are seen. The phase changes due to the $2s^{-1}3s$ Fano resonance is small for the angle-integrated photoelectron spectrum. The induced delay does not exceed ±3 as.

For the directional photoelectron spectrum, the correlation induced delay is with up to -30 as an order of magnitude larger than for the angle-integrated result as we have already found in Sec. III B 3 for residual correlation effects. In both cases (directional or angle-integrated), the delay is relatively small compared to the $2p^{-1}3s$ resonance lifetime of 6.4 fs ($\Gamma$ = 0.1 eV within TDCIS). The derivative of the absolute dipole phase, measured in FROG-CRAB, reflects the lifetime of the resonance. In our method, we measure the difference in the influence of the $2s^{-1}3s$ autoionizing state on the Rydberg states

$2p^{-1}3s$ and $2p^{-1}4s$ , which is two orders of magnitude smaller than the absolute dipole phase.

## IV. CONCLUSION AND OUTLOOK

We have proposed a new method to characterize attosecond UV pulses with the help of bound electron wave packets. Different spectral components of the UV pulse interfere as an electron can be ionized from different energy levels. This leads to quantum beats (an oscillating photoelectron signal) as function of the pulse delay. We showed that angle integration eliminates the influence of the dipole phase in the photoelectron spectrum, which becomes critical for pulses with duration below 100 as.

Rydberg wave packets have favorable properties for the proposed method. The energy spacing between electronic states decreases with $1/n^3$ offering high spectral energy resolution and the possibility to bridge energy regions with no spectral weights (as in the case of pulse trains). The downside of using Rydberg state is the small photoionization cross section leading to weak signal strengths. Multi-level wave packets open up the possibility for consistency checks of the retrieved phases—a feature that does not exist in other pulse reconstruction techniques.

We studied the role of correlation effects. We found the dipole phase cannot be completely eliminated by angle-integration. The effect is, however, much weaker than the changes in the Wigner delay and the IR-induced continuum–continuum delay. Particularly Rydberg wave packets minimize correlation effects. We have shown in potassium and neon correlation effects result indeed in negligible phase corrections.

When vibrational Rydberg-like wave packets instead of electronic ones are used and the pulse spectrum is fully known, this approach can be turned around and be used to probe non-Born-Oppenheimer dynamics. Correlated electronic-vibrational motions results in an extra phase contribution, which is equivalent to the dipole phase dependence in atoms due to electronic correlations.

We believe ionizing Rydberg wave packets is a versatile approach to determine the spectral phases of complex pulses, e.g. generated by table-top attosecond laboratories or FEL facilities. We have focused here on pulses in the UV regime. This technique can be easily extended to x-rays with shorter wavelengths and into the optical and near-infrared domains with longer wavelengths.

As pulses durations approach the zeptosecond regime [53], ionization from different inner shells cannot be distinguished anymore making established attosecond pulse characterization techniques more prone to error [54]. Our method is not affected by inner-shell ionization. Together with the spectral phase accuracy and the applicability to a very broad spectral ranges, we believe this approach offers several key properties for characterizing the next generation of attosecond pulses.

## ACKNOWLEDGMENTS

We thank Eva Lindroth and Stefan Haessler for stimulating discussions. We acknowledge the support of the Kavli Institute of Theoretical Physics (National Science Foundation under Grant No. NSF PHY11-25915) and NORDITA for support during the workshop on 'Control of Ultrafast Quantum Phenomena'. S.P. is funded by the Alexander von Humboldt Foundation and by the NSF through a grant to ITAMP. J.M.D. is funded by the Swedish Research Council, Grant No. 2014-3724.

[1] Ian A. Walmsley and Christophe Dorrer, "Characterization of ultrashort electromagnetic pulses," Adv. Opt. Photon. **1**, 308–437 (2009).

[2] M. Hentschel, R. Kienberger, Ch. Spielmann, G. A. Reider, N. Milosevic, T. Brabec, P. Corkum, U. Heinzmann, M. Drescher, and F. Krausz, "Attosecond metrology," Nature **414**, 509 – 513 (2001).

[3] P. M. Paul, E. S. Toma, P. Breger, G. Mullot, F. Augé, Ph. Balcou, H. G. Muller, and P. Agostini, "Observation of a train of attosecond pulses from high harmonic generation," Science **292**, 1689–1692 (2001).

[4] Ferenc Krausz and Misha Ivanov, "Attosecond physics," Rev. Mod. Phys. **81**, 163–234 (2009).

[5] E. Goulielmakis, M. Uiberacker, R. Kienberger, A. Baltuska, V. Yakovlev, A. Scrinzi, Th. Westerwalbesloh, U. Kleineberg, U. Heinzmann, M. Drescher, and F. Krausz, "Direct measurement of light waves," Science **305**, 1267–1269 (2004).

[6] Kun Zhao, Qi Zhang, Michael Chini, Yi Wu, Xiaowei Wang, and Zenghu Chang, "Tailoring a 67 attosecond pulse through advantageous phase-mismatch," Opt. Lett. **37**, 3891–3893 (2012).

[7] Michael Chini, Kun Zhao, and Zenghu Chang, "The generation, characterization and applications of broadband isolated attosecond pulses," Nature Photonics **8**, 178–186 (2014).

[8] Y. Mairesse and F. Quéré, "Frequency-resolved optical gating for complete reconstruction of attosecond bursts," Phys. Rev. A **71**, 011401 (2005).

[9] J. Gagnon, E. Goulielmakis, and V.S. Yakovlev, "The accurate frog characterization of attosecond pulses from streaking measurements," Appl. Phys. B **92**, 25–32 (2008).

[10] He Wang, Michael Chini, Sabih D Khan, Shouyuan Chen, Steve Gilbertson, Ximao Feng, Hiroki Mashiko, and Zenghu Chang, "Practical issues of retrieving isolated attosecond pulses," Journal of Physics B: Atomic, Molecular and Optical Physics **42**, 134007 (2009).

[11] Michael Chini, Steve Gilbertson, Sabih D. Khan, and Zenghu Chang, "Characterizing ultrabroadband attosecond lasers," Opt. Express **18**, 13006–13016 (2010).

[12] M. Lewenstein, Ph. Balcou, M. Yu. Ivanov, Anne

L'Huillier, and P. B. Corkum, "Theory of high-harmonic generation by low-frequency laser fields," Phys. Rev. A **49**, 2117–2132 (1994).

[13] A. L. Cavalieri, N. Muller, Th. Uphues, V. S. Yakovlev, A. Baltuska, B. Horvath, B. Schmidt, L. Blumel, R. Holzwarth, S. Hendel, M. Drescher, U. Kleineberg, P. M. Echenique, R. Kienberger, F. Krausz, and U. Heinzmann, "Attosecond spectroscopy in condensed matter," Nature **449**, 1029–1032 (2007).

[14] M. Schultze, M. Fiess, N. Karpowicz, J. Gagnon, M. Korbman, M. Hofstetter, S. Neppl, A. L. Cavalieri, Y. Komninos, Th. Mercouris, C. A. Nicolaides, R. Pazourek, S. Nagele, J. Feist, J. Burgdorfer, A. M. Azzeer, R. Ernstorfer, R. Kienberger, U. Kleineberg, E. Goulielmakis, F. Krausz, and V. S. Yakovlev, "Delay in photoemission," Science **328**, 1658–1662 (2010).

[15] K. Klünder, J. M. Dahlström, M. Gisselbrecht, T. Fordell, M. Swoboda, D. Guénot, P. Johnsson, J. Caillat, J. Mauritsson, A. Maquet, R. Taïeb, and A. L'Huillier, "Probing single-photon ionization on the attosecond time scale," Phys. Rev. Lett. **106**, 143002 (2011).

[16] D Guénot, D Kroon, E Balogh, E W Larsen, M Kotur, M Miranda, T Fordell, P Johnsson, J Mauritsson, M Gisselbrecht, K Varjù, C L Arnold, T Carette, A S Kheifets, E Lindroth, A L'Huillier, and J M Dahlström, "Measurements of relative photoemission time delays in noble gas atoms," Journal of Physics B: Atomic, Molecular and Optical Physics **47**, 245602 (2014).

[17] Caryn Palatchi, J M Dahlström, A S Kheifets, I A Ivanov, D M Canaday, P Agostini, and L F DiMauro, "Atomic delay in helium, neon, argon and krypton," Journal of Physics B: Atomic, Molecular and Optical Physics **47**, 245003 (2014).

[18] A. S. Kheifets, "Time delay in valence-shell photoionization of noble-gas atoms," Phys. Rev. A **87**, 063404 (2013).

[19] C.-H. Zhang and U. Thumm, "Electron-ion interaction effects in attosecond time-resolved photoelectron spectra," Phys. Rev. A **82**, 043405 (2010).

[20] S Nagele, R Pazourek, J Feist, K Doblhoff-Dier, C Lemell, K Tőkési, and J Burgdörfer, "Time-resolved photoemission by attosecond streaking: extraction of time information," Journal of Physics B: Atomic, Molecular and Optical Physics **44**, 081001 (2011).

[21] J M Dahlström, A L'Huillier, and A Maquet, "Introduction to attosecond delays in photoionization," Journal of Physics B: Atomic, Molecular and Optical Physics **45**, 183001 (2012).

[22] G. Laurent, W. Cao, I. Ben-Itzhak, and C. L. Cocke, "Attosecond pulse characterization," Opt. Express **21**, 16914–16927 (2013).

[23] L. R. Moore, M. A. Lysaght, J. S. Parker, H. W. van der Hart, and K. T. Taylor, "Time delay between photoemission from the $2p$ and $2s$ subshells of neon," Phys. Rev. A **84**, 061404 (2011).

[24] Renate Pazourek, Johannes Feist, Stefan Nagele, and Joachim Burgdörfer, "Attosecond streaking of correlated two-electron transitions in helium," Phys. Rev. Lett. **108**, 163001 (2012).

[25] J. M. Dahlström, T. Carette, and E. Lindroth, "Diagrammatic approach to attosecond delays in photoionization," Phys. Rev. A **86**, 061402 (2012).

[26] Johannes Feist, Oleg Zatsarinny, Stefan Nagele, Renate Pazourek, Joachim Burgdörfer, Xiaoxu Guan, Klaus Bartschat, and Barry I. Schneider, "Time delays for attosecond streaking in photoionization of neon," Phys. Rev. A **89**, 033417 (2014).

[27] J. Mauritsson, T. Remetter, M. Swoboda, K. Klünder, A. L'Huillier, K. J. Schafer, O. Ghafur, F. Kelkensberg, W. Siu, P. Johnsson, M. J. J. Vrakking, I. Znakovskaya, T. Uphues, S. Zherebtsov, M. F. Kling, F. Lépine, E. Benedetti, F. Ferrari, G. Sansone, and M. Nisoli, "Attosecond electron spectroscopy using a novel interferometric pump-probe technique," Phys. Rev. Lett. **105**, 053001 (2010).

[28] Renate Pazourek, Maurizio Reduzzi, Paolo A. Carpeggiani, Giuseppe Sansone, Mette Gaarde, and Kenneth Schafer, "Ionization delays in few-cycle-pulse multiphoton quantum-beat spectroscopy in helium," Phys. Rev. A **93**, 023420 (2016).

[29] Jhih-An You, Nina Rohringer, and Jan Marcus Dahlström, "Attosecond photoionization dynamics with stimulated core-valence transitions," Phys. Rev. A **93**, 033413 (2016).

[30] Harald Friedrich, *Theoretical Atomic Physics*, 3rd ed. (Springer-Verlag, Berlin, 2006).

[31] Anthony F. Starace, in *Encyclopedia of Physics*, Vol. 31: Corpuscles and Radiation in Matter I, edited by W. Mehlhorn (Springer, Berlin, 1982) Chap. Theory of Atomic Photoionization, pp. 1–121.

[32] V.O. Lorenz and S.T. Cundiff, "Ultrafast spectroscopy of a dense potassium vapor," Chemical Physics **341**, 106 – 112 (2007), ultrafast Dynamics of Molecules in the Condensed Phase: Photon Echoes and Coupled ExcitationsA Tribute to Douwe A. Wiersma.

[33] V. O. Lorenz, S. Mukamel, W. Zhuang, and S. T. Cundiff, "Ultrafast optical spectroscopy of spectral fluctuations in a dense atomic vapor," Phys. Rev. Lett. **100**, 013603 (2008).

[34] National Institute of Standards and Technology, `http://www.nist.gov/pml/data/atomspec.cfm`.

[35] Edwin E. Salpeter Hans A. Bethe, *Quantum Mechanics of One- and Two-Electron Atoms* (Springer US) iSBN: 978-0-306-20022-9 (Print) 978-1-4613-4104-8 (Online).

[36] A. D. Shiner, C. Trallero-Herrero, N. Kajumba, H.-C. Bandulet, D. Comtois, F. Légaré, M. Giguère, J-C. Kieffer, P. B. Corkum, and D. M. Villeneuve, "Wavelength scaling of high harmonic generation efficiency," Phys. Rev. Lett. **103**, 073902 (2009).

[37] Loren Greenman, Phay J. Ho, Stefan Pabst, Eugene Kamarchik, David A. Mazziotti, and Robin Santra, "Implementation of the time-dependent configuration-interaction singles method for atomic strong-field processes," Phys. Rev. A **82**, 023406 (2010).

[38] S. Pabst, L. Greenman, A. Karamatskou, Y.-J. Chen, A. Sytcheva, O. Geffert, R. Santra–XCID program package for multichannel ionization dynamics, DESY, Hamburg, Germany, 2015, Rev. 2127.

[39] A pseudo-spectral grid with a radial box size of 120 $a_0$, 750 grid points, and a mapping parameter of $\zeta = 0.5$ are used. There is no complex absorbing potential. The splitting function starts around $R_{\rm split} = 70\ a_0$, a smoothness of 2 $a_0$, and splitting interval of $dt_{\rm split} = 2$ a.u. The maximum angular momentum is 2 and Hartree-Fock (HF) orbitals up to an energy of 5 $E_h$ are considered. The propagation method is Runge-Kutta 4 with a time step $dt = 0.05$ a.u.

[40] Antonia Karamatskou, Stefan Pabst, Yi-Jen Chen, and Robin Santra, "Calculation of photoelectron spectra within the time-dependent configuration-interaction singles scheme," Phys. Rev. A **89**, 033415 (2014).

[41] T. Mazza, A. Karamatskou, M. Ilchen, S. Bakhtiarzadeh, A. J. Rafipoor, P. O/'Keeffe, T. J. Kelly, N. Walsh, J. T. Costello, M. Meyer, and R. Santra, "Sensitivity of nonlinear photoionization to resonance substructure in collective excitation," Nat Commun **6** (2015).

[42] Stefan Pabst, Daochen Wang, and Robin Santra, "Driving rabi oscillations at the giant dipole resonance in xenon," Phys. Rev. A **92**, 053424 (2015).

[43] J M Dahlström and E Lindroth, "Study of attosecond delays using perturbation diagrams and exterior complex scaling," Journal of Physics B: Atomic, Molecular and Optical Physics **47**, 124012 (2014).

[44] I. Lindgren and J. Morrison, *Atomic Many-Body Theory*, 2nd ed., Series on Atoms and Plasmas (Springer-Verlag, New York Berlin Heidelberg, 1986).

[45] M. Ya. Amusia, *Atomic photoeffect* (Plenum Press, New York, 1990).

[46] Stefan Pabst, Loren Greenman, Phay J. Ho, David A. Mazziotti, and Robin Santra, "Decoherence in attosecond photoionization," Phys. Rev. Lett. **106**, 053003 (2011).

[47] Stefan Pabst and Robin Santra, "Strong-field many-body physics and the giant enhancement in the high-harmonic spectrum of xenon," Phys. Rev. Lett. **111**, 233005 (2013).

[48] Tenio Popmintchev, Ming-Chang Chen, Dimitar Popmintchev, Skirmantas Alisauskas, Giedrius Andriukaitis, Tadas Balciunas, Audrius Pugzlys, Andrius Baltuska, Margaret Murnane, and Henry Kapteyn, "Bright coherent attosecond-to-zeptosecond kiloelectronvolt x-ray supercontinua," in *CLEO:2011 - Laser Applications to Photonic Applications* (Optical Society of America, 2011) p. PDPC12.

[49] M.C. Kohler, T. Pfeifer, K.Z. Hatsagortsyan, and C.H. Keitel, "Frontiers of atomic high-harmonic generation," *Advances in Atomic, Molecular, and Optical Physics*, Adv. At., Mol., Opt. Phys. **61**, 159 – 208 (2012).

[50] O. Zatsarinny and S. S. Tayal, "Photoionization of potassium atoms from the ground and excited states," Phys. Rev. A **81**, 043423 (2010).

[51] A pseudo-spectral grid with a radial box size of 220 $a_0$, 1000 grid points, and a mapping parameter of $\zeta = 0.5$ are used. The splitting function starts around $R_{\text{split}} = 170\ a_0$, a smoothness of 2 $a_0$, and splitting interval of $dt_{\text{split}} = 1$ a.u. The maximum angular momentum is 3 and Hartree-Fock orbitals up to an energy of 10 $E_h$ are considered. The propagation method is Runge-Kutta 4 with a time step $dt = 0.05$ a.u.

[52] Elisabeth Heinrich-Josties, Stefan Pabst, and Robin Santra, "Controlling the $2p$ hole alignment in neon via the $2s$-$3p$ fano resonance," Phys. Rev. A **89**, 043415 (2014).

[53] Tenio Popmintchev, Ming-Chang Chen, Dimitar Popmintchev, Paul Arpin, Susannah Brown, Skirmantas Ališauskas, Giedrius Andriukaitis, Tadas Balčiunas, Oliver D. Mücke, Audrius Pugzlys, Andrius Baltuiška, Bonggu Shim, Samuel E. Schrauth, Alexander Gaeta, Carlos Hernández-García, Luis Plaja, Andreas Becker, Agnieszka Jaron-Becker, Margaret M. Murnane, and Henry C. Kapteyn, "Bright coherent ultrahigh harmonics in the kev x-ray regime from mid-infrared femtosecond lasers," Science **336**, 1287–1291 (2012).

[54] Private discussions with Jens Biegert.